Water exit dynamics of buoyant spheres

Tadd T. Truscott*
Department of Mechanical and Aerospace Engineering, Utah State University, Logan, Utah 84322, USA

Brenden P. Epps
Thayer School of Engineering, Dartmouth College, Hanover, New Hampshire 03755, USA

Randy H. Munns
Department of Mechanical Engineering, Brigham Young University, Provo, Utah 84602, USA
(Received 21 March 2016; published 1 November 2016)

Buoyant spheres released below the free surface can rise well above the surface in a phenomenon known as pop-up. Contrary to intuition, increasing the release depth sometimes results in a lower pop-up height. We present the pop-up height of rising buoyant spheres over a range of release depths (1–12.5 diameters) and Reynolds numbers (4×10^4 to 6×10^5). While the dynamics of rising buoyant spheres and bubbles has been thoroughly investigated for Reynolds numbers below 10^4, pop-up in these larger-Reynolds-number regimes has not been studied. Yet the underwater motions of the sphere for the Reynolds numbers we study are the key to understanding the pop-up height. Two major regimes are apparent: vertical and oscillatory. The vertical regime exhibits a nearly vertical underwater trajectory and results in the largest pop-up heights. The oscillatory regime exhibits an underwater trajectory with periodic lateral motions and results in lower pop-up heights; this periodic lateral motion is modulated by unsteady vortex shedding in the wake of the sphere. Despite these complex fluid structure interactions, the experiments presented herein yield extremely repeatable results.

DOI: 10.1103/PhysRevFluids.1.074501

I. INTRODUCTION

Anyone who has taken a buoyant ball into a swimming pool has inevitably pulled the ball under the water surface and released it. Upon release, the ball quickly rises up through the water, breaches the free surface, and ultimately rises to some maximum height above the surface.[1]

Many school children have tested this in swimming pools by releasing air filled balls under water and testing if the pop-up height is increased by simply taking the ball to deeper depths. These young experimentalists quickly discover that sometimes, releasing the ball deeper results in the ball coming to the surface and skimming across it rather than rising up into the air. Counterintuitively, a larger release depth sometimes leads to a *decreased* pop-up height. Herein, we unravel this mystery through high-speed imaging and particle image velocimetry observations.

The pop-up problem consists of three interrelated problems: buoyancy-driven rising sphere (under surface), surface breaching (at surface), and the pop-up height (above surface). In this article, we focus on the above-surface portion of the problem and in particular the pop-up height, as that has received very little attention in the literature.

This canonical pop-up problem is of fundamental interest in applications where objects breach the free surface. Marine life breaches the free surface for various purposes. For example, penguins exit the water after a hunt or to avoid predators. It has been hypothesized that emperor penguins

*Correspondence should be addressed to taddtruscott@gmail.com; www.splashlab.org

[1]P. Bourrier *et al.* [1] coined this phenomenon the *pop off effect*, but we will refer to it as *pop-up* as the term *pop off* is sometimes used colloquially to denote shooting a gun or speaking angrily.

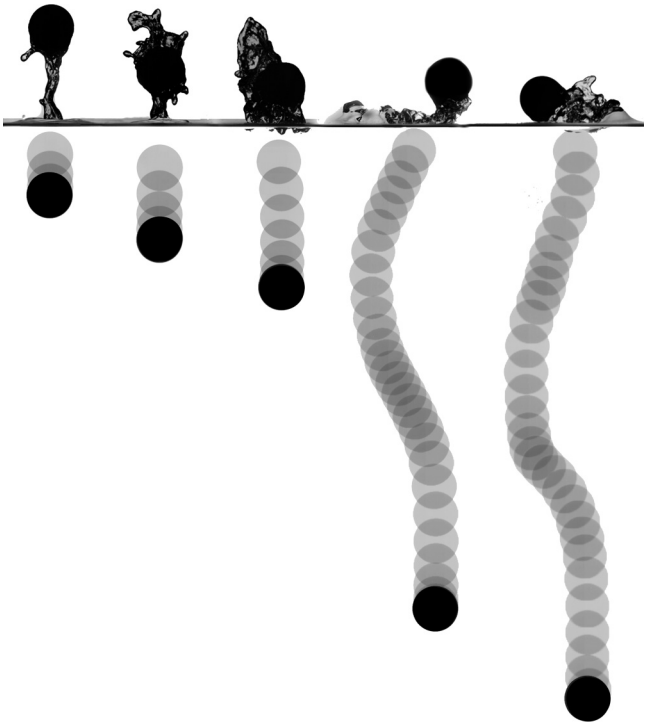

FIG. 1. Images of maximum pop-up heights ($h_p/D = 2.2, 1.1, 0.9, 0.9, 0.5$) for buoyant spheres (ping pong balls) released from varying depths ($h_d/D = 1.5, 2.5, 3.5, 10.5, 12.5$), with height and depth measured from the undisturbed free surface to the sphere center. Trajectories are shown below the free surface as superimposed transparent images 20 ms apart.

use bubbles released from their feathers during ascent in order to reduce drag and increase exit velocity and pop-up height [2]. Great white sharks may breach the free surface to catch their prey (seals, who breach to try to escape); sharks have been observed to rise above the water surface by as much as 3 m [3]. Of course, whale breaching is likely the most popular image that comes to mind, although their motivation is not conclusively known [4]. Dolphins breach the free surface during travel to reduce drag or during social behavior [5]. Synthetic objects also breach the water surface. For instance, an emergency blow is a maneuver in which a submarine is aimed toward the surface and the buoyancy-regulating bladders are emptied with high-pressure air, propelling the submarine to the surface with buoyancy as the driving force [6]. Certain classes of missiles have also been designed to launch from submarines and be propelled with an initial velocity sufficient to breach the free surface after which the primary rocket motor ignites [7]. Other important applications of the pop-up effect include underwater vehicle exit [8], missile exit [9–11], wave-energy converters, and floating sea structures.

Spheres represent a canonical object for studying the pop-up problem, since the geometry is simple and the object is driven to the surface only by the force of buoyancy. However, the fluid dynamics are far from simple. Prior to breach, an ascending sphere may experience a nonvertical trajectory depending on the release depth, as shown in Fig. 1. This deviation from a completely vertical trajectory is due to asymmetric vortex shedding [12]. Depending on the Reynolds number ($\mathrm{Re} \equiv \rho V D/\mu$) during ascent, these vortices will develop and shed differently, leading to three underwater trajectory regimes: vertical, oblique, and oscillatory [12]. While the dynamics of motion and wake formation of buoyant spheres has received considerable attention in the past 20 years, past studies have focused on low Reynolds number and neglected the physics of the pop-up.

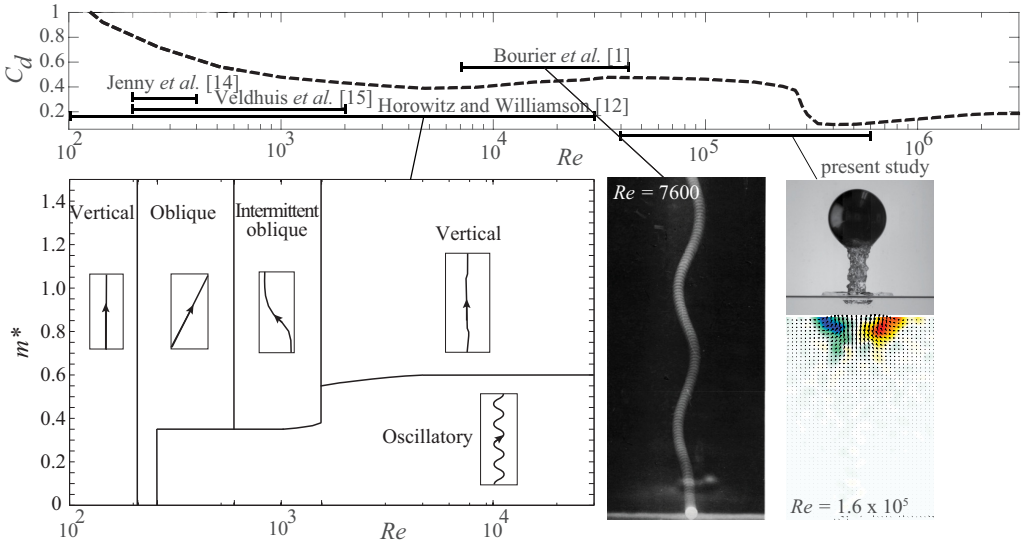

FIG. 2. Shown on top are the steady drag coefficient data (- - -) from [13] that illustrate the Reynolds number Re regimes of past experiments [1,12,14–16] and the present study, whose ranges are indicated by —. On the left is the mass ratio $m^* \equiv \rho_s/\rho$ versus Reynolds number, redrawn from the work of Horowitz and Williamson [12], who studied both ascending ($m^* < 1$) and descending ($m^* > 1$) spheres. The images are relative to marked Reynolds numbers: stroboscopic image from Bourrier *et al.* [1] (middle), free surface breach (right upper) correlated with PIV vorticity fields just below the free surface after breach (right lower).

Figure 2 shows ranges of Re in the studies of past researchers as well as the Re considered herein. The inset plot in Fig. 2 is redrawn after Horowitz and Williamson [12] and defines the trajectory regimes based on mass ratio $m^* \equiv \rho_s/\rho$ and Reynolds number Re. Whereas past researchers have covered Re below 3×10^4, the present study considers Re ranging between 4×10^4 and 6×10^5. We note that their study also included falling spheres where the density ratio was greater than unity and include it here for completeness.

The pop-up height depends on the free-surface exit speed, which in turn depends on the trajectory regime and the dynamics during surface breach. As the sphere breaches the water surface, a thin layer of water is lifted above the surface on top of the sphere, which then flows down the sides of the sphere [17]; at the same time, the low-pressure wake region under the sphere draws a portion of the free surface down to form a depression around the sphere. Depending on the Froude number ($\mathrm{Fr} \equiv V^2/gD$) and Weber number ($\mathrm{We} = \rho V^2 D/\sigma$) during water exit, as well as the vortex structures shed near the water surface, the resulting cavity and splash plume will take on various shapes, indicating varying amounts of energy transferred to the fluid during breach.

Moran [18] reviewed mathematical theories of water entry and exit (e.g., potential flow theory with linearized boundary conditions and added mass theory) and concluded that no theories at that time yielded accurate predictions of the loads experienced by a body during water exit; he suggested that the problem be analyzed by a computational fluid dynamics (CFD) solution to the Navier-Stokes equations. Furthermore, Greenhow [19] compared a two-dimensional (2D) numerical simulation of water exit to added mass theory and concluded that added mass theory provides a poor prediction of forces during water exit, since added mass theory ignores viscous effects (vortices behind the body, which deform the free surface) and gravitational effects (free surface deformation at finite Froude number). The conclusion that simple added mass theory is insufficient to describe water breach is confirmed in the results of Zhu *et al.* [20]. A number of researchers have since performed CFD simulations of 2D cylinders and wedges breaching the water surface at a constant prescribed speed [21–24]. Korobkin *et al.* [8] considers the problem of a 3D symmetric body being lifted out

of the water, with the body initially floating on the water surface (i.e., no vortical wake present during breach). They show a favorable comparison between a potential flow simulation (ignoring gravity and modeling the body surface pressure using the linearized unsteady Bernoulli equation $p - p_{atm} = -\rho\partial\phi/\partial t$) and a full viscous simulation in OPENFOAM. Our conclusion is that for high-Reynolds-number water exit, potential flow theory could describe the dynamics of water exit if the vortical structures in the wake of the sphere were known and accurately modeled. Simple added mass models (which ignore the vortical structures in the wake) do not suffice, nor do models that ignore free-surface deformations. No completely 3D viscous simulations have been performed of the water exit problem and no simulations have been performed of a sphere freely rising through the free surface under the action of buoyancy. The experimental results presented herein will be valuable to future researchers embarking on such simulations.

Relative to the underwater trajectories and the surface breach, the pop-up height has received very little attention in the literature. The pop-up problem essentially is a synthesis of the underwater trajectory problem and the surface breach problem. Ignoring air resistance, once the sphere has cleared the water, the only force acting on the sphere is gravity. So the pop-up height is simply determined by a transfer of kinetic energy to potential energy of the sphere after clearing the surface. However, the speed (and thus kinetic energy) of the sphere after it has cleared the surface is dictated both by the speed at which it approaches the surface (set by the underwater dynamics) and the change in speed during breach. As a synthesis and combination of these individual problems, determining the pop-up height as a function of release depth and sphere properties is an interesting and challenging physics problem, worthy of theoretical, computational, and experimental consideration. Herein, we present highly accurate experimental data for the pop-up height that can be used as validation data in future theoretical and computational studies.

In this paper, the pop-up height above the free surface of a rising buoyant sphere is examined. Experimental correlations between pop-up height versus release depth will be drawn for spheres of varying diameters and materials. Behavior of the trajectory of each sphere will be examined during ascent and breach of the free surface in order to discuss regime classification based solely on physical paths. In order to further explore the physics behind the trajectory and pop-up of a sphere, 2D particle image velocimetry (PIV) is performed and visualization of the vortex structures formed by an ascending sphere is presented. Size and behavior of vortex structures relative to the size and path of the sphere will give insight into the overall motion of a sphere. Finally, exit velocities are calculated and correlated with pop-up height. Section II elaborates on the theoretical discussion presented thus far. Section III presents the experimental methods used herein. Section IV provides the experimental results and discussion and Sec. V summarizes the conclusions drawn in this study.

II. THEORY

A. Dimensional analysis

This problem exhibits an unusual dimensional analysis, because there are no externally imposed velocity or time scales. The pop-up height h_p is defined as the maximum height attained by the center of the sphere above the undisturbed free surface. The pop-up height is to be determined as a function of the primary parameters of the problem: $h_p = f(h_d, D, \rho_s, \rho, \mu, \sigma, g)$, where h_d is the release depth (of center of sphere below free surface), D is the sphere diameter, ρ_s is the sphere density, ρ is the fluid density, μ is the fluid dynamic viscosity, σ is the fluid surface tension, and g is gravity. Choosing D, ρ, and g as the repeating variables, dimensionless groups are formed as follows:

$$\frac{h_p}{D} = \phi\left(\frac{h_d}{D}, m^* \equiv \frac{\rho_s}{\rho}, \mathrm{Ar} \equiv \frac{(\rho - \rho_s)\rho g D^3}{\mu^2}, \mathrm{Bo} \equiv \frac{(\rho - \rho_s) g D^2}{\sigma}\right), \tag{1}$$

where m^* is the mass ratio, Ar is the Archimedes number, and Bo is the Bond number. Since the sphere is driven to the surface by the net force of buoyancy minus weight, another relevant nondimensional number would be $(\mathcal{B} - \mathcal{W})/\mathcal{B} = (\rho - \rho_s)/\rho = 1 - m^*$, where $\mathcal{B}$ denotes buoyancy and $\mathcal{W}$ weight.

The Archimedes number is interpreted in either of the two following ways. First, for a sphere traveling at speed V, the interpretation is

$$\begin{aligned}\mathrm{Ar} &= \frac{(\rho-\rho_s)gD^3}{\mu V D}\frac{\rho V^2 D^2}{\mu V D}\\ &= \frac{\mathcal{F}_{\text{net buoyancy}}}{\mathcal{F}_{\text{viscous}}}\frac{\mathcal{F}_{\text{inertial}}}{\mathcal{F}_{\text{viscous}}},\end{aligned} \tag{2}$$

where $\mathcal{F}_{\text{net buoyancy}}$ denotes net buoyancy force, $\mathcal{F}_{\text{viscous}}$ viscous force, and $\mathcal{F}_{\text{inertial}}$ inertial force. A second interpretation is achieved by forming an argument for this arbitrary speed V as follows: In a high-Reynolds number flow, the terminal velocity of the sphere is reached when the net buoyancy force $(\rho-\rho_s)gD^3$ balances the pressure force $\rho V^2 D^2$, which gives a velocity scale $V^2 \sim (\rho-\rho_s)gD/\rho$. The Archimedes number can then be interpreted as the square of the Reynolds number at this hypothetical velocity. The Archimedes number also occurs in sedimentation problems to characterize the settling of particles in a fluid under the action of gravity.[2] The pop-up problem herein is analogous to the sedimentation problem, except that the particles considered herein are buoyant spheres that rise instead of fall.

Note that since there is no imposed velocity scale in the problem, the Reynolds number and Froude number do not explicitly appear in the nondimensionalization (1). Nevertheless, for a sphere traveling at arbitrary speed V, the Reynolds number ($\mathrm{Re} \equiv \rho V D/\mu$), Froude number ($\mathrm{Fr} \equiv V^2/gD$), and Weber number ($\mathrm{We} = \rho V^2 D/\sigma$) can be computed. We will make use of the Reynolds number to calculate terminal velocity and the Froude number to calculate pop-up height.

B. First-order physics

The ascent of a rising buoyant sphere can be modeled with a simple force balance as follows:

$$(m+m_a)a = F_b - F_g - F_d, \tag{3}$$

where $m = \rho_s \frac{4}{3}\pi R^3$ is the sphere mass, $m_a = \rho \frac{2}{3}\pi R^3$ is the added mass, $a = \dot{V}$ is the sphere acceleration (positive upward), $F_b = \rho g \frac{4}{3}\pi R^3$ is the buoyancy force, $F_g = mg$ is the sphere weight, $F_d = \frac{1}{2}\rho V^2 C_d A$ is the drag force, $A = \pi R^2$ is the cross-sectional area, $C_d(\mathrm{Re})$ is the drag coefficient at the instantaneous Reynolds number, R is the sphere radius, and V is the instantaneous velocity of the sphere. Decoupling the quasisteady drag and added mass forces is an approximation akin to Morrison's formula, which is justifiable considering that the added mass force occurs immediately in response to accelerations and the quasisteady drag term arises some time later after viscous effects alter the boundary layer and wake structure [25]. The quasisteady viscous drag F_d model is understood to fail in the case of unsteady vortex shedding; nevertheless, Eq. (3) can be used to estimate the terminal velocity, assuming steady motion.

The terminal velocity V_t is obtained from (3) by setting $a = 0$ and solving for the velocity:

$$V_t^2 = \frac{\frac{4}{3}(\rho-\rho_s)gD}{\rho C_{d_t}}. \tag{4}$$

Equation (4) is implicit, since C_{d_t} is a function of terminal velocity through the terminal Reynolds number $\mathrm{Re}_t = \rho V_t D/\mu$. However, Eq. (4) can be rearranged to give the terminal Reynolds number Re_t in terms of the Archimedes number Ar as follows:

$$\mathrm{Re}_t^2 C_{d_t} = \tfrac{4}{3}\mathrm{Ar}. \tag{5}$$

---

[2]The Archimedes number is analogous to the Grashof number $\mathrm{Gr} \equiv \beta(T-T_\infty)\rho^2 g D^3/\mu^2$, which occurs in natural convection problems, where the density difference is imposed by local thermal heating $\{(\rho-\rho_\infty) = \beta(T-T_\infty)\rho\}$ rather than a difference in density between body and fluid as herein.

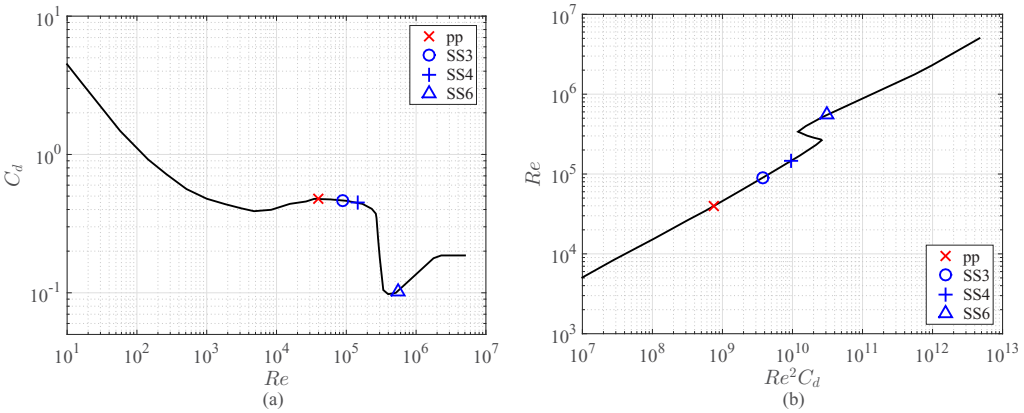

FIG. 3. Terminal Reynolds number and drag coefficient: (a) C_d versus Re experimental data from [13] for a smooth sphere in steady flow and (b) Re versus $\mathrm{Re}^2 C_d$ using the data from (a). Given Ar, (b) yields Re and then (a) yields C_d. Symbols show the terminal Reynolds numbers achieved in this experiment, as well as the resulting drag coefficients.

For a given sphere, Ar is known and thus (5) determines $\mathrm{Re}_t^2 C_{d_t}$. Given $C_d(\mathrm{Re})$ data [Fig. 3(a)], one can form a table of Re versus $\mathrm{Re}^2 C_d$ [Fig. 3(b)] and determine Re_t from $\mathrm{Re}_t^2 C_{d_t}$. This is illustrated graphically in Fig. 3. Figure 3 shows the terminal Reynolds numbers achieved in this experiment, as well as the resulting drag coefficients. Table I lists the physical characteristics of the spheres used in this study and Table II provides the results of terminal velocity calculations using Eqs. (4) and (5).

The pop-up height h_p can be estimated by balancing the kinetic energy of the sphere at its terminal velocity $\frac{1}{2} m V_t^2$ with its potential energy at the pop-up height mgh_{p_t}, which yields

$$\frac{h_{p_t}}{D} = \frac{1}{2}\frac{V_t^2}{gD} = \frac{2}{3}\frac{(1-m^*)}{C_{d_t}}. \tag{6}$$

This energy balance is quite dubious: (i) It assumes that the sphere velocity after exit of the free surface is still equal to the estimated terminal velocity; (ii) the terminal velocity is an estimate and is quite dubious, because it ignores unsteady vortex shedding; (iii) the energy balance ignores the kinetic energy of the fluid both before and after water exit (for a sphere moving at speed V in an infinite fluid, the kinetic energy of the fluid would be $\frac{1}{2} m_a V^2$); (iv) the energy balance ignores the kinetic and potential energy of the water in the splash plume; and (v) the energy balance ignores the work done on the sphere as it breaches the surface.

Equation (6) can be generalized to give the pop-up height for any given vertical speed at breach

$$\frac{h_p}{D} = \frac{1}{2}\frac{V^2}{gD}. \tag{7}$$

The theoretical model embodied by Eq. (3) can be simulated numerically using Euler's method to find V as follows. Assume that the sphere is released from rest $V^{(0)} = 0$ at depth $z^{(0)} = -h_d$ (i.e., $\zeta^{(0)} = z^{(0)} + h_d = 0$). At each time step, compute Re, interpolate C_d from the data in Fig. 3(a), compute F_d, compute a from (3), and then integrate forward in time $V^{(k)} = V^{(k-1)} + a\,\delta t$ and $z^{(k)} = z^{(k-1)} + V^{(k-1)}\,\delta t$. This results in a $V(\zeta)$ curve and the breach velocity simply is $V(\zeta = h_d)$. The pop-up height for any release depth $h_p(h_d)$ can be estimated by substituting $V(h_d)$ into (7). The results of this calculation (using $\delta t = 0.0001$) are shown as dashed lines in Fig. 5. These curves asymptote to the terminal pop-up heights predicted by (6). These theoretical predictions are also plotted as dashed lines in Figs. 8(d) and 8(e), which show (vertical) breach velocity (plotted nondimensionally as the Froude number V^2/gD) versus release depth h_d. These theoretical reference

predictions match poorly with the experimental data in both Figs. 5 and 8, showing that this reference model, i.e., quasisteady drag and purely vertical trajectory, is not a good description of reality.

C. Trajectory regimes

Contrary to popular thought and intuition, increasing the depth of release does not necessarily result in a higher pop-up height. The pop-up height depends on the free-surface exit speed, but this speed is not necessarily an increasing function of release depth. In particular, for large enough release depths, vortex shedding events may occur that affect the trajectory and speed of the sphere.

A number of authors have considered the underwater dynamics of freely rising spheres [1,12,14,16,26]. Figure 2 summarizes the ranges of Reynolds numbers achieved in these studies. In this figure, the observed terminal velocity was used to calculate the Reynolds number. For context, the steady-state drag coefficient C_d versus Re data [13] is shown, illustrating that all prior studies considered laminar flow.

Before continuing, we must pause and justify why we chose to illustrate the literature parametrized by the Reynolds number, even though Re does not appear in (1) as a true nondimensional parameter of the problem. Horowitz and Williamson [12] argue that even though the Reynolds number does not appear explicitly in the nondimensionalization (1), the Reynolds number still governs the vortex shedding behavior and thus the trajectory of the sphere. In other words, they assume that the vortex shedding dynamics depend only on the relative speed of the sphere and the fluid, not whether the sphere is forced to rise by buoyancy or forced by being attached to a test fixture immersed in a freestream. This argument is somewhat tenuous, because a freely rising buoyant sphere does not have constant vertical speed like the sphere in a wind tunnel does. Nevertheless, we follow Horowitz and Williamson and present this section using ostensibly a time-averaged Re.

While the nomenclature of the regimes of a rising buoyant sphere varies in the literature, the actual behavior does not. All researchers generally agree upon the following four regimes: vertical, oblique, intermittent oblique, and oscillatory. Additionally, Jenny *et al.* [14] and Veldhuis *et al.* [15,16] report a fourth, chaotic regime, with random out-of-plane motion. Sir Isaac Newton also reported a chaotic trajectory of objects free falling from the dome of St. Paul's Cathedral [27]. We now know that nonvertical trajectories are caused by vortex shedding, and Horowitz and Williamson [12] claim that chaotic (out of plane) behavior is due to lack of quiescence in the fluid. Considering the range $10^3 < \mathrm{Re} < 10^4$, Horowitz and Williamson [12] show that for a given Reynolds number, the lightest spheres (low m^*) oscillate, whereas more dense spheres (large m^*) rise vertically in a straight line, as expected.

While the dynamics of motion and wake formation have received considerable attention in the past 20 years, these studies have focused on subsurface dynamics while completely neglecting pop-up. Additionally, no previous work has investigated the characteristics of buoyant rising spheres in high-Re regimes.

III. METHODS

A. Experimental setup

In order to assess the sphere trajectory and pop-up height, high-speed cameras were used to image the ascent from release to the apex of the pop-up. Particle image velocimetry was used to qualitatively assess the vortex structures shed during ascent and approach to the free surface. Figure 4 is an illustration of the experimental setup. For each trial, the sphere was set to a specified depth in the center of a tank filled with water; the sphere was held in place by a suction cup tethered by flexible tubing to a syringe. After a sufficient wait time to allow the water to become quiescent, the syringe was depressed, releasing the sphere. The rising sphere was imaged during ascent, breach of the free surface, and pop-up above the surface. The sphere was then reset to the desired depth and the water allowed to settle for the next release. In order to produce a meaningful statistical sample, ten iterations were performed at each release depth. Release depths h_d (measured from the

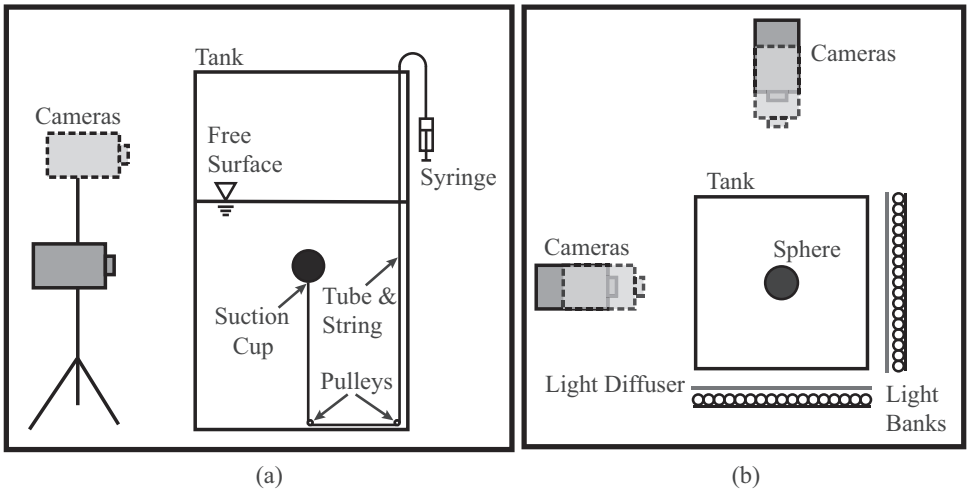

FIG. 4. Illustration of the experimental setup: (a) side view and (b) top view. A suction cup in (a) keeps the sphere below the surface until release. Four cameras record the motion (two underwater and two above the free surface). Cameras are placed orthogonal to one another (a) with large light banks providing back lighting.

undisturbed free surface to the center of the sphere) were incremented in half diameters to a depth of approximately ten diameters.

The physical characteristics of the spheres used in this study are shown in Table I. Four spheres were chosen of differing varying mass ratio and diameter in order to span larger values of terminal Reynolds number than considered by past researchers. The terminal Reynolds numbers listed in Table II ($0.39 \times 10^5 \leqslant \mathrm{Re} \leqslant 5.51 \times 10^5$) are estimated using Eq. (5) and steady-state drag coefficient data for a smooth sphere. The stainless steel spheres used were hollow and of nominal diameters, 3, 4, and 5.87 (roughly 6) in., and these will be referred to as SS3, SS4, and SS6, respectively. These shells are approximately 0.5 mm thick, have a mirrorlike polish, and is manufactured by welding two hemispheres together and then ground and polished. A standard ping pong ball was also used and will be referred to as PP. Multiple trials with each of the four spheres at each of several release depths yielded for this study 664 total trials. The surface roughness of each of the spheres

TABLE I. Physical characteristics of spheres used in the present work. Spheres SS3, SS4, and SS6 are hollow stainless steel spheres with diameters 3.00, 4.01, and 5.87 (roughly 6) in. and PP is a standard ping pong ball. Here D is the sphere diameter, $R = D/2$ the sphere radius, m the sphere mass, $m^* \equiv \rho_s/\rho$ the mass ratio, ψ the sphericity (Sec. III C 2), r_c the radial distance of the center of mass from the center of sphere (Sec. III C 3), ϵ the root mean square roughness, Ar the Archimedes number (1), Bo the Bond number (1), and h_d the release depth (measured from the free surface to the center of the sphere). Release depths h_d/D increment in half diameters (664 total trials). The assumed properties of water at temperature $T = 20\,^\circ$C are as follows: density $\rho = 998.2$ kg/m^3, dynamic viscosity $\mu = 1.002 \times 10^{-3}$ kg/m s, kinematic viscosity $\nu = 1.003 \times 10^{-6}$ m^2/s, and surface tension $\sigma = 0.0728$ N/m.

Sphere	D (cm)	m (kg)	m^*	ψ (%)	r_c/R (%)	$\epsilon/D \times 10^6$	Ar $\times 10^{-8}$	Bo	h_d/D	Trials
PP	3.97	0.0027	0.083	99 ± 1.1	0.49 ± 0.12	103 ± 1.5	5.6	194	1–12.5	10
SS3	7.62	0.0802	0.347	97 ± 1.2	0.11 ± 0.01	5.27 ± 1.0	28.2	510	1–10.5	10
SS4	10.2	0.1718	0.312	98 ± 0.6	1.23 ± 0.07	3.72 ± 0.33	70.6	958	1–10.5	10
SS6	14.9	0.4906	0.283	99 ± 0.4	0.39 ± 0.02	1.92 ± 0.08	232	2149	1–6.5	2

TABLE II. Terminal velocity calculations using Eqs. (4)–(6) as well as the data in Fig. 3.

Sphere	Ar $\times 10^{-8}$	$\mathrm{Re}_t \times 10^{-5}$	C_{d_t}	V_t (m/s)	Fr_t	We_t	h_{p_t}/D
PP	5.6	0.39	0.48	1.00	2.55	539	1.28
SS3	28.2	0.90	0.47	1.18	1.87	1461	0.94
SS4	70.6	1.45	0.45	1.43	2.04	2835	1.02
SS6	232	5.51	0.10	3.71	9.39	28115	4.72

was determined using a profilometer in the manner reported in [28]. The length of the path was 4.8 mm and averaged rms values are reported in Table I.

Water temperature during the experiments was measured in the range $18.6\,^{\circ}\mathrm{C} < T < 24.7\,^{\circ}\mathrm{C}$. All results herein are nondimensionalized assuming the following water properties corresponding to $T = 20\,^{\circ}\mathrm{C}$ (standard temperature): $\rho = 998.2\ \mathrm{kg/m^3}$, $\mu = 1.0016 \times 10^{-3}\ \mathrm{kg/m\,s}$, $\nu = 1.0034 \times 10^{-6}\ \mathrm{m^2/s}$, and $\sigma = 0.0728\ \mathrm{N/m}$.

B. Image acquisition and processing

Referring to Fig. 4, further details of the experimental setup and image acquisition are as follows. Four synchronized cameras imaged side views perpendicular to two sides of the tank, above and below the free surface. The cameras were calibrated for parallax using a standard grid image technique. Fluorescent light banks provided back and side lighting in order to increase contrast. Consistent release depths were controlled by a pulley clutch system with a laser level marking the top of the sphere. The spheres were submerged, held in place, and released using a suction cup, tube, and syringe to create a vacuum. The glass tank measured $81.3 \times 81.3 \times 182.9\ \mathrm{cm^3}$ and held approximately 806 L of water. High-speed cameras (Photron FastCam SA-3) recorded images at 1000 frames per second (fps) with a resolution of 1024×1024 for the (above water) pop-up images and 512×1024 for the underwater trajectories from release to free surface. The field of view for the pop-up images was $52 \times 52\ \mathrm{cm^2}$ (yielding a 19.7 pixels $\mathrm{cm^{-1}}$ magnification) and the field of view for the trajectory images was $47 \times 94\ \mathrm{cm^2}$ (yielding a 10.9 pixels $\mathrm{cm^{-1}}$ magnification).

Data extraction from the raw high-speed images was performed through image processing of the trajectory and pop-up event. Position data were extracted from the raw high-speed images using a sphere tracking image processing algorithm. Underwater position data were collected until 1/8 of the sphere remained visible below the free surface. Velocity and acceleration were inferred from the position data; after applying a second-order polynomial fit to the position data, first and second derivatives of the fitted curve produced the velocity and acceleration data, respectively. These data were interpolated to yield the velocity of the sphere at the free surface.

Particle image velocimetry experiments were performed following the same and release methods and experimental process outlined for the pop-up data. Raw images were captured at 1000 fps in a fluid with polyamide seeding particles illuminated by a laser sheet from a class 4, 527-nm YLF laser pulsed at 500 Hz (frame straddling) with a time spacing dt between 10 and 30 ms depending on the speed of the rising sphere. Postprocessing was performed using a LAVISION software package. Vector fields are presented with vectors showing velocity magnitude and vorticity shown as the vector background color ω_z.

C. Experimental considerations

1. Quiescent fluid

Quiescent fluid is desirable to provide consistent test conditions and hence accurate and repeatable experimental results. However, since 664 trials were performed in the present study, determining the minimum acceptable wait time between trials for quiescence was worthwhile. Horowitz and

Williamson [12] suggest that a wait time of 2 h is needed, but they do not give justification for this choice. In order to determine the required wait time, a 2D two-component PIV experiment was performed (with each of the spheres). Following an experimental run and resetting the sphere, PIV images were captured every 5 min for 1 h. Results show that after 30 min, the measured PIV velocity is approximately that of the settling speed of the PIV particles. Thus, a 30-min wait time was used herein.

2. Sphericity

Sphericity quantifies the roundness of an object. The sphericity of an object is the ratio of the surface area of a sphere with the same volume as the object divided by the actual surface area of the object [29]. That is, $\psi = 4\pi(3\mathcal{V}/4\pi)^{2/3}/\mathcal{A}$, where ψ is the sphericity, $\mathcal{V}$ is the volume of the object, and $\mathcal{A}$ is the surface area of the object. An ideal sphere would have a sphericity of $\psi = 1$ (i.e., 100%). Sphericity measurements are reported in Table I. All four spheres show high sphericity, as desired.

3. Center of mass

Jenny *et al.* [14] showed that induced motion (i.e., oblique oscillatory rather than oblique steady, or chaotic rather than oscillatory) could be initiated with a nonhomogeneous sphere. They showed this in numerical simulations by adding a small imperfection to the model that produced a center of mass that was initially horizontal with the geometric center, resulting in an initial rotation. The deviation of center of mass from the sphere center was determined experimentally via the following procedure, which consists of finding the location of the static pole of the sphere by allowing it to come to rest after a rotational perturbation. By marking the location of the static polar axis the sphere can then be released from various rotational angles (on the surface of the water) and allowed to rotate. By calculating the angular acceleration and mass moment of inertia we can estimate the center of mass by $l = I\alpha/mg$. The results are shown in Table I and reveal that the spheres are susceptible to induced motion as described by Jenny *et al.* [14]. In order to reduce bias in the experimental results, orientation of the sphere at release was selected at random.

IV. RESULTS

We began our study by addressing the question of how the pop-up effect varies with depth. Here we present the pop-up heights associated with different release depths and show that they are directly related to the underwater trajectories, which are a result of vortices shed in the wake of the rising spheres.

Presentation of data and results throughout this section will be correlated with the three regimes of motion experienced by a rising buoyant sphere: vertical, oblique, and oscillatory as represented in Fig. 2. The vertical regime is defined by a nearly vertical trajectory with almost no deviation in the horizontal direction. The oblique regime is defined by a straight but not quite vertical trajectory during ascent. We consider the oblique regime a transition between the vertical and oscillatory regimes for these high-Re spheres. Spheres ascending in the oscillatory regime follow a periodic trajectory that is vertical in the mean with lateral oscillations.

A. Pop-up height

Figure 5 reveals the relationship between pop-up height h_p/D versus release depth h_d/D for each of the spheres in the present study. The error bars are reported with a 95% confidence interval on the mean using a t distribution based on ten runs at each depth in Figs. 5(a)–5(c) and two runs at each depth in Fig. 5(d). Note the extremely small width of the error bars, demonstrating the astounding repeatability of these experiments. The largest error bars occur at release depths where the sphere undergoes large oscillations below the free surface prior to water exit.

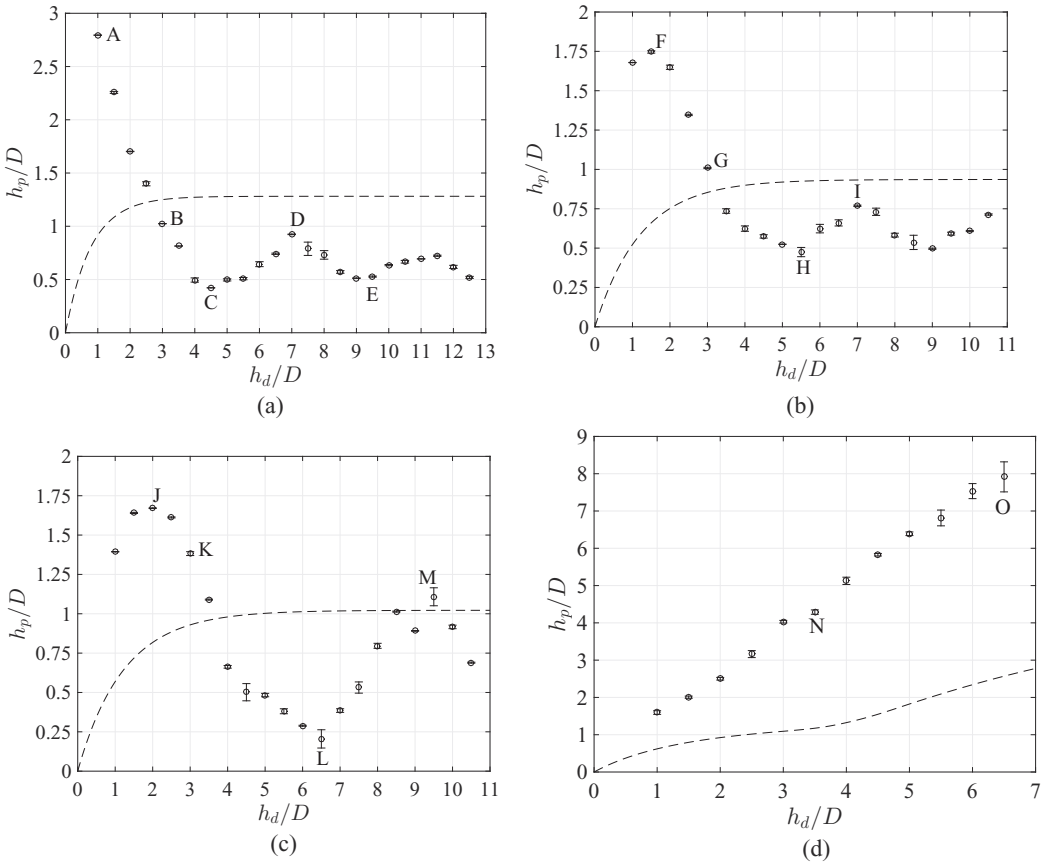

FIG. 5. Pop-up height h_p versus release depth h_d normalized by sphere diameter D for each of the four cases in the present study. The error bars are reported with a 95% confidence interval on the mean using a t-distribution based on (a)–(c) ten runs and (d) two runs. The dashed line represents the pop-up height predicted by quasisteady simulation [Eq. (7)], which asymptotes to the terminal pop-up height. Capital letters A–O represent cases of interest in later figures: (a) PP, $m^* = 0.083$; (b) SS3, $m^* = 0.347$; (c) SS4, $m^* = 0.312$; and (d) SS6, $m^* = 0.283$.

Figures 5(a)–5(c) show a common pattern of alternating local maximum and minimum pop-up heights; this pattern is due to vortex shedding and the oscillatory nature of the trajectory of the sphere during ascent toward the free surface. For each of the maximum pop-up heights in Fig. 5, a correlated image is shown in Fig. 6. For the PP, SS3, and SS4 spheres, the maximum pop-up heights were reached when the sphere was released from a shallow depth ($h_d/D = 1$, 1.5, and 2 for the PP, SS3, and SS4 spheres, respectively), and these cases are denoted by A, F, and J. The lowest pop-up heights occurred when the sphere was released from larger depths ($h_d/D = 4.5$, 5.5, and 6.5 for the PP, SS3, and SS4 spheres, respectively), and these cases are denoted by C, H, and L. Following the occurrence of a local minimum pop-up height, increased release depths lead to increasing pop-up heights, resulting in another local maximum pop-up height at $h_d/D = 7$, 7, and 9.5 (labeled cases D, I, and M). The pop-up heights for cases I and M are lower than those for F and J, respectively, showing that the local maximum peak is smaller for a greater release depth than for a shallow release depth. This pattern is repeated with peaks and troughs as the release depth increases.

In addition, Fig. 7 shows a time series from below the surface to the maximum pop-up height for cases F–I in Fig. 5(b). These images reveal the sphere rising through the water to the free surface and

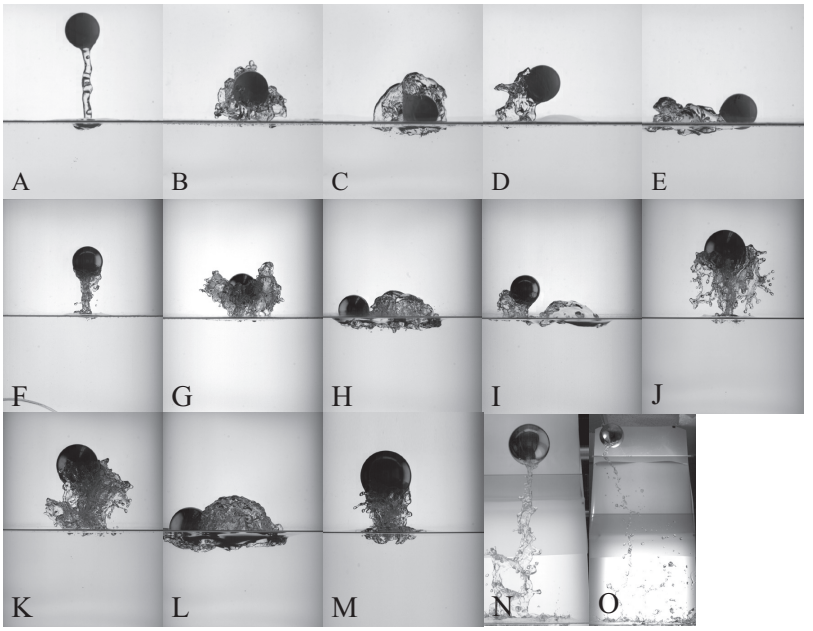

FIG. 6. Images of the breach height apex corresponding to the pop-up and release height data in Fig. 5 (e.g., cases A–O). See [30] for video 1-3 showing the entire time series for cases A–E, F–I, and N and O, respectively.

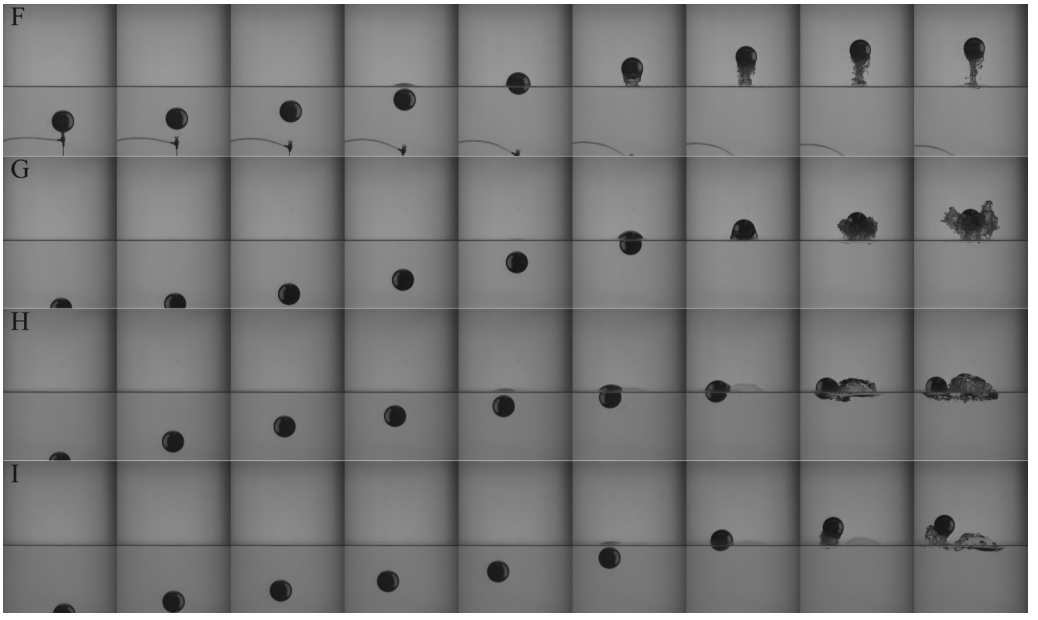

FIG. 7. Image sequence of an ascending 3-in. stainless steel sphere from four different release depths: $h_d/D = 1,2.5,5,6.5$ (F–I). The images were captured at 1000 fps. The far right image depicts the maximum height or apex for the individual time series and respective release depths. The maximum pop-up heights are $h_p/D = 2.25,1.51,0.98,1.27$ (F–I). The time step between images in each time series is $dt = 39,41,51,59$ ms (F–I). See [30] for video 2 showing the entire time series for F–I.

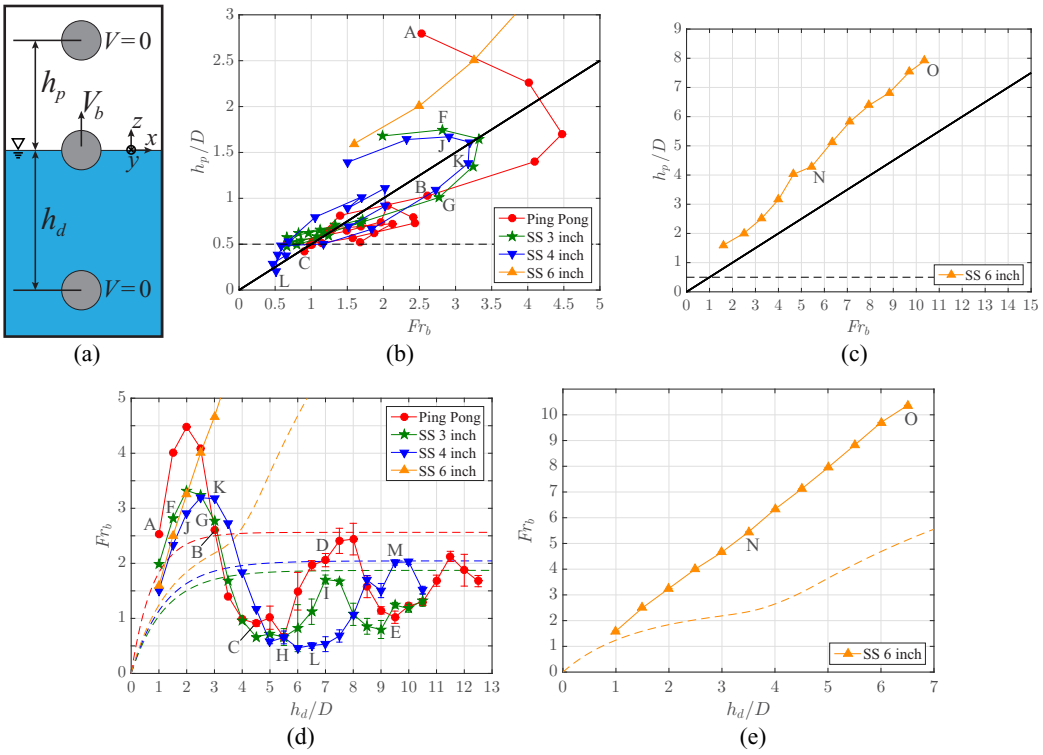

FIG. 8. (a) Drawing of the energy balance estimation in Eq. (8). (b) and (c) Pop-up height h_p/D versus breach Froude number $\mathrm{Fr}_b = V_b^2/gD$ for (b) all spheres and release depths and again for (c) SS6, where V_b is the vertical velocity at breach. Error bars on h_p (not shown) are the same as in Fig. 5. The theoretical estimate in Eq. (8) is represented by — in (b) and (c). The horizontal dashed line in (b) and (c) is the height needed for the bottom of the sphere to clear the free surface. (d) and (e) Breach Froude number Fr_b versus release depth h_d/D for (d) all spheres and (e) SS6. The theoretical estimate of the Froude number (nondimensional vertical velocity) predicted using Euler's method (Sec. II B) is represented by dashed colored lines.

then traveling through it to varying maximum heights while carrying varying amounts of attached liquid. As the maximum pop-up height decreases the amount of water that is brought up with the sphere appears to increase.

B. Froude number at breach

A rough estimate for the pop-up height can be obtained by considering the sphere at breach [Fig. 8(a)]. Breach is defined herein to be the instant when the center of the sphere is at the undisturbed free surface. Assuming no work is done on the sphere by the fluid during breach (i.e., zero net hydrodynamic force acting on the sphere), a simple balance of sphere kinetic energy at breach and potential energy at the pop-up height yields

$$\frac{h_p}{D} = \frac{1}{2}\mathrm{Fr}_b, \tag{8}$$

where we have defined $\mathrm{Fr}_b = V_b^2/gD$ as the Froude number and V_b is the vertical velocity at breach. Equation (8) ignores the work done by buoyancy and dynamic pressure forces, as well as energy lost to lifting a portion of the water, splash, and wave production. These are expected to be significant, so (8) merely serves as a reference to explain the general trend in the data.

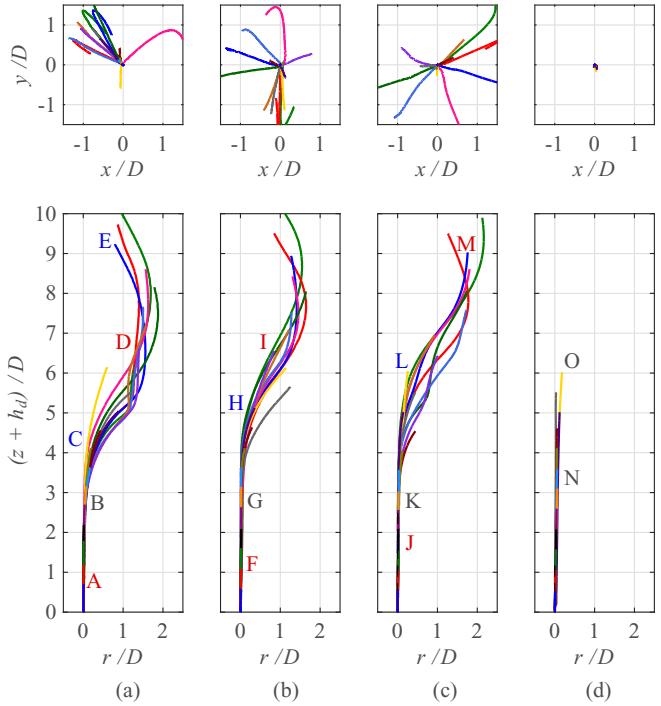

FIG. 9. Trajectories are shown on top in the x-y plane and on bottom plotted as shifted vertical position $(z + h_d)/D$ versus radial position $r = \sqrt{x^2 + z^2}$. This figure shows one representative trajectory for each sphere, from left to right: ping pong, SS3, SS4, and SS6. Note that since each release depth has been shifted to the bottom of the figure, the free surface is at different heights for each of the different cases shown.

Figure 8(b) shows the pop-up height versus breach Froude number for all spheres and release depths in the current study. The data points shown are averages over all of the trials performed at each submerged depth. The breach velocity V_b is determined from the image sequences via a second-order fit to a time sequence of position data. Cases that are in the accelerating regime (i.e., A, B, F, G, J, K, N, and O) do not collapse as well as those in the oscillatory regimes, which seem to follow the relationship of (8). The SS6 data are unique because it spans a much larger Fr regime. The SS6 cases have not yet met the upper limit of the breach height (limited by the experimental setup) and as such they all fall above the prediction of (8). These accelerating cases breach to greater heights because the vortices formed in the wake are not yet fully developed, as will be shown in Sec. IV D.

C. Trajectories below the free surface

Trajectories below the free surface have been the focus of much of the research performed in the past on rising buoyant spheres. Bourrier *et al.* [1], Jenny *et al.* [14], Veldhuis and Biesheuvel [16], and Horowitz and Williamson [12] based the prediction and definition of regimes experienced by rising buoyant spheres upon the nature of the path below the free surface. We observed regimes similar to those discussed by Bourrier *et al.* [1] due to the similarity of Reynolds and Froude numbers between our studies.

Figure 9 shows the trajectory of one representative trial at each release depth, with all trajectories superimposed upon one another. In Fig. 9 (bottom panel), we plot sphere height above release point $(z + h_d)/D$ versus radial deviation from the release position $r/D = \sqrt{x^2 + y^2}/D$. (Since $z = 0$ at the free surface, $z + h_d = 0$ at the release point.) In this way, the behavior of the rising sphere is

keyed to the release point. The free surface appears at different heights in Fig. 9 for the different release depths.

The most striking and important feature of Fig. 9 is that the underwater trajectories are roughly the same regardless of release depth. The path of the sphere's first few diameters of travel displays the vertical regime with very little deviation from the centerline during ascent. As the sphere travels further, the transition to an oscillatory regime is observed as the sphere leaves the centerline and follows an oscillatory path.

In Fig. 9 (top panel), we plot the top view of position y/D versus x/D. This figure reveals that the trajectory of each sphere lies in some plane as it travels upward, but the chosen plane is arbitrary, consistent with previous observations [12,14,16,31]. Other researchers have observed spiral or chaotic trajectories, but Horowitz and Williamson [12] claim that these chaotic trajectories are due to ambient turbulence in the test tank.

The onset of the vortex-induced motions, the catalyst of the transition to and existence of the oscillatory regime, appears earlier for spheres with a low mass ratio m^*, as reported by Jenny *et al.* [14]. This claim is supported and confirmed here at these higher Re number cases by the onset of oscillation at $(z + h_d)/D = 3$ for the PP case ($m^* = 0.08$), compared to 4 for the SS3 ($m^* = 0.35$) and SS4 ($m^* = 0.31$) cases.

The oscillatory path of a sphere will vary the velocity vector upon arrival at the free surface, shedding light on the variation of pop-up height above the free surface for a range of release depths. The trajectory angles are near vertical for shallow release depths, allowing higher pop-up heights. For example, the PP case of Fig. 9 begins to transition from vertical to oblique near $(z + h_d)/D > 2$, which corresponds to decreased pop-up heights as h_d/D increases in Fig. 5(a). For the SS3 and SS4 cases a similar trend is apparent, however, it seems that release depths less than 1.5 and 2, respectively, increase to the maximum. Likely, this is due to a maximization in acceleration from a competition between the buoyant force and the developing drag in the wake. Buoyancy always acts to accelerate the sphere upward. Drag continually increases as the sphere ascends and gains speed, during which a vortical wake develops. Discrete vortex shedding events are associated with linear impulses applied to the sphere, which change the sphere's linear momentum (both slow the sphere and redirect it laterally). As this occurs the sphere slows down, the wake is shed momentarily, and the sphere is pushed toward the opposite side.

Once the sphere has transitioned into the oscillatory regime, the angle of trajectory at the free-surface exit varies greatly along with the resulting pop-up height depending on the release depth. A sphere released from one particular release depth will result in consistent pop-up heights with very low error. For instance, the ping pong data of Fig. 9 show large deviations in radial trajectory occurring around $h_d/D = 4.5$, which corresponds to the lowest pop-up heights of C in Fig. 5(a). From this point the pop-up height increases with release depth up to another local maximum at case D, corresponding to $h_d/D = 7$ in Fig. 9 where the trajectory is nearly vertical. This trend continues but is only shown up to $h_d/D = 10$ for the PP case of Fig. 9. The trend is similar for cases SS3 and SS4.

The trajectories for the 6-in. stainless steel sphere (SS6) reveal that the sphere remains in the vertical regime for all of the release depths presented (Fig. 9). The deepest releases appear to reach the initial stages of the transition to the oblique regime, evidenced by the slight deviations in the figure. However, the experimental pop-up data in Fig. 5(d) reveals an increase in pop-up height even for the largest release depths. Based on the small radial deviation from the central y axis, it is possible to hypothesize that the SS6 case is in the beginning stages of the oblique regime and it would follow that the curve of the pop-up height data in Fig. 5(d) would begin to plateau instead of following a continual linear increase with release depth.

The limited release depth of the SS6 experiments (because of the limited size of the glass tank) led to an attempt to collect data at a swimming pool with the SS6 and a 12-in.-diam stainless steel hollow sphere. Spheres released in the swimming pool instantly began to oscillate vigorously during ascent, even at shallow release depths. This early onset of the oscillatory regime is due to the ambient turbulence in the water (a condition common to a swimming pool), adding to the importance of

consistent experimental conditions through quiescent fluid. As a result, the current study is unable to draw conclusions about the maximum pop-up height of the SS6 case from experimentation.

D. PIV and vortex shedding

Past research has shown the role that wake formation and vortex shedding play in the oscillatory path of a rising buoyant sphere. Veldhuis and Biesheuvel [16] give a thorough description of wake formation and structures of a sphere held fixed in a uniform flow, where the wake is symmetric at low Re and transitions from oscillatory laminar shedding to turbulent as Re increases. Horowitz and Williamson [32] performed visualization experiments and PIV measurements of the vortical structures left in the wake of a rising sphere. Visualization was performed on freely rising spheres and PIV was performed on a tethered sphere in a computer-controlled tow tank. These studies resulted in the discovery of patterns and wake modes unlike any found previously for either fixed or vibrating spheres [32]. This section continues the discussion of regimes through presenting results of 2D PIV of rising spheres near the free surface. As previously noted, values of Re for the current study is significantly higher than those in past studies.

1. Vertical regime

As previously discussed, spheres in the vertical regime demonstrate a completely vertical path during ascent. Cases F and J correspond to maximum pop-up heights. Figures 10(a) (case F) and 11(a) (case J) illustrate the wake formed behind the sphere just after release. At this early stage of wake development, separation from the sphere has not yet occurred and the vorticity in the wake is small in magnitude and mainly is located near the sphere body. The small amount of vorticity in the flow is an indication of a lower resistance than the larger wakes we will discuss later. While viscous drag is present, pressure drag is minimal due to the lack of wake separation and vortex shedding. Given these conditions, the sphere experiences very little resistance to the upward motion and achieves the greatest pop-up heights ($h_p/D = 1.75, 1.67$). The yellow-green structure behind the sphere in Fig. 10(a) is not a wake from the sphere but rather the suction cup falling after release (we mask the spheres for the PIV processing but did not mask the suction cup release mechanism). While the wake dynamics of the vertical regime may seem trivial, PIV visualization of the wake formation and separation sheds light on why the sphere motion is vertical, explained by the small wake and lack of flow separation, and why the resistive forces are so small.

Two more PIV cases are shown in Fig. 12 (cases N and O) of a SS6 in the vertical regime. Although wake formation for cases N and O is much more developed than those of cases F and J, the pop-up height is significantly higher. The Re_b of cases N and O ($\mathrm{Re}_b = 3.76 \times 10^5$ and 5.19×10^5, respectively) is significantly larger than those of cases F and J ($\mathrm{Re}_b = 0.99 \times 10^5$ and 1.55×10^5, respectively). The larger Reynolds numbers of the SS6 cases puts this sphere in the turbulent regime, allowing the wake to separate much farther back on the sphere (120°) as compared to spheres within the laminar regime (82°) and thus reducing significantly the drag coefficient $C_d(\mathrm{Re})$. The change in angle at which wake separation occurs for a turbulent case significantly reduces the pressure drag on a rising sphere, allowing the sphere to exit the free surface at a much greater velocity resulting in more dramatic pop-up heights.

The wake structure behind the sphere in case N [Fig. 12(a)] is uniform and symmetric, justifying a completely vertical trajectory during ascent in the vertical regime. The wake of the sphere in case O [Fig. 12(b)] displays asymmetry with a vortex forming on the left side of the sphere. This small vortex contributes to a slightly oblique angle in the vertical trajectory as shown previously in Fig. 9 (SS6), suggesting that the sphere is beginning to transition from the vertical regime into the oblique or oscillatory regime. While the trajectory gives evidence of the oblique regime, as defined by trajectories and pop-up data for spheres of lower Re (laminar), the pop-up height does not. For spheres rising in the laminar regime, an oblique vertical trajectory reduces the pop-up height. In contrast, the experimental data presented here show that an oblique trajectory does not necessarily

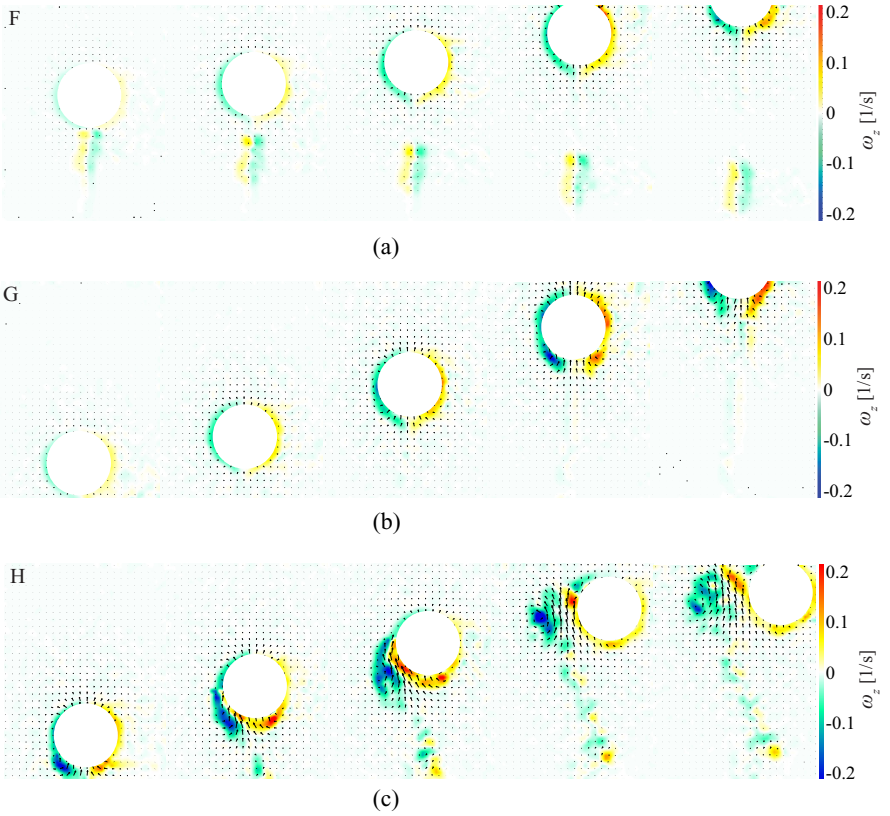

FIG. 10. Time series of PIV vector and vorticity fields for individual trials representative of the cases labeled in Fig. 5. Here h_p/D is the pop-up height from Fig. 5, δt is the time step between frames, and $\mathrm{Re}_b = V_b D/\nu$ is the breach Reynolds number computed using the measured breach speed V_b. The free surface is roughly at the top of the frame. In case F, the yellow-green structure behind the sphere is not a wake from the sphere but rather the suction cup falling after release. In case H, a vortex has formed near the back of the sphere and is in the process of shedding as the sphere approaches the free surface. See [30] for video 2 showing the entire time series. (a) Representative case F: SS3, $h_d/D = 1.5$, $h_p/D = 1.75$, $\mathrm{Re}_b = 0.99 \times 10^5$, and $\delta t = 20$ ms. (b) Representative case G: SS3, $h_d/D = 3.0$, $h_p/D = 1.01$, $\mathrm{Re}_b = 0.98 \times 10^5$, and $\delta t = 30$ ms. (c) Representative case H: SS3, $h_d/D = 5.5$, $h_p/D = 0.47$, $\mathrm{Re}_b = 0.48 \times 10^5$, and $\delta t = 24$ ms.

reduce pop-up height. Our limitations in depth prevent us from studying this effect, but could be the subject of a future study.

Figures 10(b) (case G) and 11(b) (case K) show PIV results corresponding to cases of spheres attaining somewhat less than the maximum pop-up height. They have lower pop-up heights because the wake has larger vortical structures, which exert a lower-pressure region (larger drag force) on the sphere during breach. The figures confirm this, as do the decreased pop-up heights ($h_p/D = 1.01, 1.38$). In both cases G and K, the vortical structures have not yet detached from the back of the sphere but appear to be stronger on the left-hand side than the right and are the likely cause of the slight oblique angle in the vertical trajectory and slower exit speeds.

2. Oscillatory regime

Figure 10(c) (case H) reveals a large vortex structure on the left of the sphere. The structure is on the order of the size of the sphere and forces the sphere to the right in time. Case H ($h_d/D = 5.5$) results in a pop-up height of 0.47. The sphere is released from rest and enters the bottom of the

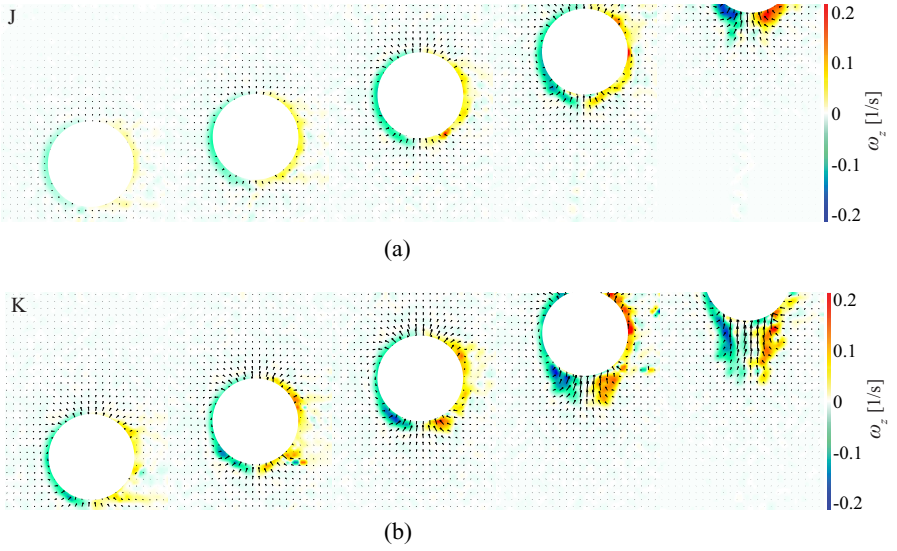

FIG. 11. Time series of PIV vector and vorticity fields. The legend is the same as in Fig. 10. See [30] for video 3 showing the entire time series. (a) Representative case J: SS4, $h_d/D = 2.0$, $h_p/D = 1.67$, $\mathrm{Re}_b = 1.55 \times 10^5$, and $\delta t = 30$ ms. (b) Representative case K: SS4, $h_d/D = 3.0$, $h_p/D = 1.38$, $\mathrm{Re}_b = 1.62 \times 10^5$, and $\delta t = 15$ ms.

frame after rising several diameters. During ascent a large vortical structure is shed in the wake as the sphere approaches the surface and the vortices are spread outward, no longer symmetric. The vortical structure is shed just before the sphere leaves the surface, causing the sphere to leave the plane of the laser in the far right image moving into the frame. This causes the sphere to move out

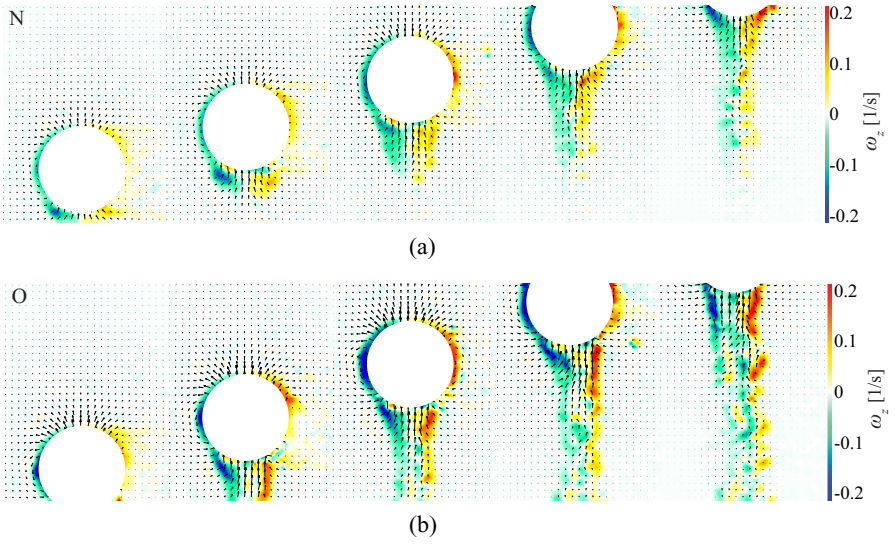

FIG. 12. Time series of PIV vector and vorticity fields. The legend is the same as in Fig. 10. See [30] for video 4 showing the entire time series. (a) Representative case N: SS6, $h_d/D = 3.5$, $h_p/D = 4.29$, $\mathrm{Re}_b = 3.76 \times 10^5$, and $\delta t = 17$ ms. (b) Representative case O: SS6, $h_d/D = 6.5$, $h_p/D = 7.92$, $\mathrm{Re}_b = 5.19 \times 10^5$, and $\delta t = 13$ ms.

of the surface at an angle with a reduced speed, effectively reducing the pop-up height as captured beautifully by the high-speed camera image shown in Fig. 6 for case H. While outside the scope of this work, one might wonder what would happen if the oscillatory regime were suppressed. It is likely that the pop-up trends would be more similar to the largest sphere (SS6) and could possibly be accomplished by employing the Leidenfrost effect similar to the work of Vakarelski *et al.* [33].

V. CONCLUSION

The pop-up problem consists of three interrelated problems: under-surface motions of a buoyancy-driven rising sphere, surface breaching, and the rise above the surface to the pop-up height. Not surprisingly, the pop-up height is roughly predicted by equating kinetic energy during breach with the potential energy at pop-up. This prediction is made more accurate by including the work done on the sphere during breach as well as the potential energy lost to lifting some mass of water above the free surface during breach. These two effects are strongly dependent on the strength and configuration of the vortical wake attached to the sphere as it approaches the surface. Additionally, the pop-up height is reduced if the sphere does not approach the free surface vertically, which too is modulated by wake structure. Although the Reynolds number does not appear as an intrinsic nondimensional variable in the problem setup (1), the Reynolds number greatly affects the wake dynamics. If the Reynolds number is sufficiently large (large Archimedes number) then the rising spheres are less affected by the wake and can pop up to much greater heights. While the surface breaching problem is quite complex, the underwater motions of the sphere are relatively straightforward. The underwater trajectory is essentially independent of the release depth; regardless of release depth, the spheres essentially traverse the same trajectory, with spheres released at a larger depth traversing a greater distance along this path. Thus, release depth impacts pop-up height by setting the location along the trajectory at which the sphere encounters the free surface. Our PIV results show that the trajectory of the sphere is modulated by vortex shedding events. Since vortex shedding occurs at regular intervals, the repeatability of the experiment is very high. We note that one requirement for repeatability is quiescence in the fluid and as such swimming pools make poor experimental facilities.

ACKNOWLEDGMENTS

This material is based upon work supported by the National Science Foundation under Grant No. CMMI-1126862. T.T.T. would like to thank the Naval Undersea Warfare Center for encouraging and supporting the initial study.

[1] P. Bourrier, E. Guyon, and J. P. Jorre, The ‘pop off’ effect: Different regimes of a light ball in water, Eur. J. Phys. **5**, 225 (1984).
[2] G. Hodges, Emperor penguins: Escape velocity, Natl. Geograph. **222**(11), 60 (2012).
[3] R. A. Martin, N. Hammerschlag, R. S. Collier, and C. Fallows, Predatory behavior of white sharks (*Carcharodon carcharias*) at Seal Island, South Africa, J. Mar. Biol. Assoc. U.K. **85**, 1121 (2005).
[4] P. J. Corkeron, Humpback whales (*Megaptera novaeangliae*) in Hervey Bay, Queensland: Behavior and responses to whale-watching vessels, Can. J. Zoolog. **73**, 1290 (1995).
[5] G. Bearzi, E. Politi, and G. N. di Sciara, Diurnal behavior of free-ranging bottlenose dolphins in the Kvarneri (Northern Adriatic Sea), Mar. Mammal Sci. **15**, 1065 (1999).
[6] M. C. Bettle, A. G. Gerber, and G. D. Watt, Unsteady analysis of the six DOF motion of a buoyantly rising submarine, Comput. Fluids **38**, 1833 (2009).
[7] J. E. Fidler, U.S. Patent No. US5070761A (1991).
[8] A. Tassin, D. J. Piro, A. A. Korobkin, K. J. Maki, and M. J. Cooker, Two-dimensional water entry and exit of a body whose shape varies in time, J. Fluids Structures **40**, 317 (2013).

[9] J. Waugh and G. Stubstad, NAVWEPS Report No. 7735, 1961 (unpublished).
[10] L. Zhiyong, Y. Shuqun, Y. Kai, X. Sheng, and W. Baoshou, Numerical Simulation of Water-Exit Cavity, Fifth International Symposium on Cavitation, Osaka, 2003.
[11] X.-s. Chu, K. Yan, Z. Wang, K. Zhang, G. Feng, and W.-q. Chen, Numerical simulation of water-exit of a cylinder with cavities, in *Proceedings of the 9th International Conference on Hydrodynamics*, edited by Y. S. Wu, S. Q. Dai, H. Liu, and X. C. Yang (China Ocean, Hong Kong, 2010).
[12] M. Horowitz and C. H. K. Williamson, The effect of Reynolds number on the dynamics and wakes of freely rising and falling spheres, J. Fluid Mech. **651**, 251 (2010).
[13] B. R. Munson, T. H. Okiishi, W. W. Huebsch, and A. P. Rothmayer, *Fundamentals of Fluid Mechanics*, 7th ed. (Wiley, New York, 2013).
[14] M. Jenny, J. Dušek, and G. Bouchet, Instabilities and transition of a sphere falling or ascending freely in a newtonian fluid, J. Fluid Mech. **508**, 201 (2004).
[15] C. H. J. Veldhuis, A. Biesheuvel, and D. Lohse, Freely rising light solid spheres, Int. J. Multiphase Flow **35**, 312 (2009).
[16] C. H. J. Veldhuis and A. Biesheuvel, An experimental study of the regimes of motion of spheres falling or ascending freely in a Newtonian fluid, Int. J. Multiphase Flow **33**, 1074 (2007).
[17] P. Y. Liju, R. Machane, and A. Cartellier, Surge effect during the water exit of an axisymmetric body traveling normal to a plane interface: Experiments and BEM simulation, Exp. Fluids **31**, 241 (2001).
[18] J. Moran, Therm Advanced Research, Inc. Report No. TAR-TR 6501, 1965 (unpublished).
[19] M. Greenhow and S. Moyo, Water entry and exit of horizontal circular cylinders, Phil. Trans. R. Soc. Lond. A **355**, 551 (1997).
[20] X. Zhu, O. M. Faltinsen, and C. Hu, Water entry and exit of a horizontal circular cylinder, J. Offshore Mech. Arctic Eng. **129**, 253 (2007).
[21] G. Colicchio, M. Greco, M. Miozzi, and C. Lugni, Experimental and numerical investigation of the water-entry and water-exit of a circular cylinder, in Proceedings of the 24th International Workshop on Water Waves and Floating Bodies, Zelenogorsk, 2009 (unpublished).
[22] Y. Zhang, Q. Zou, D. Greaves, D. Reeve, A. Hunt-Raby, D. Graham, P. James, and X. Lv, A level set immersed boundary method for water entry and exit, Commun. Comput. Phys. **8**, 265 (2010).
[23] R. Panahi, Simulation of water-entry and water-exit problems using a moving mesh algorithm, J. Theor. Appl. Mech. **42**, 79 (2012).
[24] R. Rajavaheinthan and M. Greenhow, Constant acceleration exit of two-dimensional free-surface-piercing bodies, Appl. Ocean Res. **50**, 30 (2015).
[25] J. Newman, *Marine Hydrodynamics* (MIT Press, Cambridge, 1977).
[26] D. G. Karamanev and L. N. Nikolov, Free rising spheres do not obey Newton's law for free settling, AIChE J. **38**, 1843 (1992).
[27] I. Newton, *Mathematical Principles of Natural Philosophy*, translated by I. B. Cohen and A. Whitman (University of California Press, Berkeley, 1999), Vol. 3.
[28] T. Truscott and A. Techet, Water entry of spinning spheres, J. Fluid Mech. **625**, 135 (2009).
[29] H. Wadell, Volume, shape, and roundness of quartz particles, J. Geol. **43**, 250 (1935).
[30] See Supplemental Material at http://link.aps.org/supplemental/10.1103/PhysRevFluids.1.074501 for videos showing time series.
[31] R. H. Munns, Popup height and the dynamics of rising buoyant spheres, M.Sc. thesis, Brigham Young University, 2013.
[32] M. Horowitz and C. H. K. Williamson, Critical mass and a new periodic four-ring vortex wake mode for freely rising and falling spheres, Phys. Fluids **20**, 101701 (2008).
[33] I. U. Vakarelski, D. Y. C. Chan, and S. T. Thoroddsen, Leidenfrost vapour layer moderation of the drag crisis and trajectories of superhydrophobic and hydrophilic spheres falling in water, Soft Matter **10**, 5662 (2014).